4

Radiation Protection in Medical Imaging

Horaţiu Colosi[1], Dan Colosi[2], Vlad Mureşan[3] and Marius Roman[3]
[1]*Iuliu Haţieganu University of Medicine and Pharmacy, Cluj-Napoca*
[2]*State University of New York, School of Dental Medicine, Stony Brook, New York*
[3]*Technical University, Cluj-Napoca*
[1,3]*Romania*
[2]*USA*

1. Introduction

Life on Earth has developed continuously in the presence of natural radiation. Radiation is a form of energy transfer through space and matter. The ability of radiation to transfer energy at the molecular level to living organisms is at the root of current efforts to understand and limit the effects of radiation on humans.

The radiation spectrum includes forms of radiation that carry various energy levels. Radiation forms, such as x-radiation, which carry sufficient energy to overcome binding energies of electrons and to eject them from their atomic orbits, can cause the formation of ions in the matter through which they travel, and are termed ionizing radiation. Ionizing radiation may also dissociate molecular bonds, leading to the formation of free radicals.

1.1 Biologic effects of ionizing radiation

A great proportion of the effects of ionizing radiation on living matter are a result of the interaction of these forms of radiation with water, a ubiquitous molecule that is present in most tissues and organs. This interaction leads to the generation of highly reactive radical species, mainly from the hydroxyl and hydroperoxyl categories, which, in turn, can interact with cellular DNA, leading to the formation of strand breaks and base damage (Hall & Giaccia 2005). To a lesser extent, radiation can also directly ionize or damage DNA and other biologic molecules: RNA, proteins, lipids. Many occurrences of damage limited to one DNA strand are rapidly detected by the surveillance mechanisms of the cell and the DNA integrity is restored using the intact complementary DNA strand as template. However, double-strand breaks, in which an intact DNA template is not available, are more difficult to repair accurately (Mladenov & Iliakis 2011). As a result, radiation-induced DNA double strand breaks may often lead to misrepaired DNA, resulting in point mutations, deletions or chromosomal translocations. Radiation-induced DNA damage that escapes detection by cell cycle checkpoints during cellular mitosis can result in an uncontrolled, accelerated rate of mitotic division of the affected cell (Hall & Giaccia 2005), a cellular hallmark of cancer. The association between exposure to radiation and cancer induction is well documented through epidemiological studies (Ron 2003).

1.2 Radiation doses

Various quantities are used to describe the radiation dose to organisms and the resulting risk. The absorbed dose refers to the radiation energy absorbed by tissues per unit of mass. It is measured in grays (Gy), with 1 gray equivalent to 1 joule of radiation energy absorbed per kilogram.

The effective dose accounts for the type of radiation and the biologic tissue that is exposed, by applying a radiation weighting factor and a tissue-weighting factor to the absorbed dose. The radiation-weighting factor of x-radiation is one. Tissue weighting factors have been assigned to various tissues and organs based on their estimated susceptibility to radiation damage. The effective dose, measured in Sieverts (Sv), is used to estimate risks from radiation exposure. For exposures to limited parts of the body, as is often the case in medical imaging, the calculated effective dose is equivalent to the whole body exposure that carries the same risk.

	Effective radiation dose (μSv)	**Background Equivalent (days)**
Cosmic radiation	390	59
Radon and other radioactive gases	1260	190
Other terrestrial radiation	770	116
Total natural	**2.420**	1 year
Medical exposure	**600**	90
Total annual average dose	**3020**	455

Table 1. Sources of natural radiation and their average contribution to human exposure (adapted from United Nations Scientific Committee on the Effects of Atomic Radiation Report 2008)

Natural radiation contributes approximately 2.4 milliSieverts (mSv) annually to the average human radiation exposure of 3.0 mSv (United Nations Scientific Committee on the Effects of Atomic Radiation [UNSCEAR] Report 2008). Main natural sources of ionizing radiation are cosmic radiation, mainly from the sun and other stars, and terrestrial radiation, originating from naturally occurring radioactive elements (table 1).

Because the Earth's atmosphere acts as a radiation absorber and attenuator, exposure to cosmic radiation is greatly impacted by altitude. The exposure value to cosmic radiation at sea level approximately doubles with each 2000 m of elevation. While the yearly exposure to cosmic radiation at sea level is on average 0.24 mSv, at an altitude of 1600 m it is approximately 0.5 mSv. Similarly, airplane travel contributes to radiation exposure in the general population, with doses estimated to approximately 0.025 mSv for every 5 hours flown at 12,000 m (White & Pharoah, 2009).

Terrestrial radiation includes that originating from radionuclides in the soil, such as potassium 40, uranium 238 and thorium 232, some of which are taken up by ingestion. Together, these sources result in an annual dose of approximately 0.8 mSv. However, the main single source of natural radiation exposure is radon, a gas and uranium decay product, which contributes roughly 50% of the total natural radiation exposure to the general population (table 1). Radon may enter buildings through imperfectly sealed foundations

and tends to accumulate in basements, from where it may leak into adjacent living spaces. Its radioactive decay products are inhaled, taking residence in the respiratory epithelium and contributing to the occurrence of lung cancer. Radiation exposure from radon varies widely with the geologic composition throughout the world.

Human activity has led to the development of new sources of radiation over the past decades. Medical radiation is the greatest peaceful contributor to radiation exposure in the general population, with an average annual effective dose of approximately 0.6 mSv (table 1).

2. Radiation exposure and current practices for radiation protection

2.1 Radiation exposure in diagnostic imaging

Medical use of radiation has increased continuously throughout the world, irrespective of the economic level of various regions. While therapeutic use of radiation in the treatment of cancer contributes a significant amount of radiation to a small number of individuals, the use of diagnostic radiation imparts a smaller amount of radiation to a large, and constantly growing, number of individuals.

The development of computed tomography (CT) over the past few decades has revolutionized diagnostic imaging. Its use has increased exponentially, and it is estimated that in the United States more than 62 million CT scans have been performed in 2006, compared to less than 20 million in 1995, and just 3 million in 1980 (Brenner & Hall, 2007). Due to the relatively higher radiation dose from a typical CT scan compared to that from conventional imaging modalities (table 2), and due to its widespread and increasing use, medical CT is currently estimated to contribute a significant amount of radiation exposure to the general population.

	Effective Dose (μSv)	**Background Equivalent (days)**
Head plain radiograph	27 – 100	**4 – 15**
Dental radiographs (set of 19-20) *	33 – 150	**5 – 23**
Chest plain radiographs (PA + lateral)	100 – 290	**15 – 44**
Mammography	230 – 400	**35 – 123**
Abdomen plain radiograph	370 – 810	**56 – 123**
Head computed tomography	900 – 2800	**137 – 426**
Abdomen and pelvis computed tomography	3100 – 15300	**1.3 – 6.4 years**

Table 2. Medical diagnostic imaging procedures and their contribution range to patients' radiation exposure (data: United Nations Scientific Committee on the Effects of Atomic Radiation Report 2008, * White and Pharoah, 2009)

Due to the large number of CT scans being administered in the present, and the trend of this number to increase in the future, radiation exposure from CT may gain significance as a public health concern (Brenner and Hall, 2007).

As a result, current radiation safety efforts carry a significant focus on monitoring and limiting medical radiation exposure from CT to the general population.

2.2 Radiation protection measures in diagnostic imaging

The main concern from medical imaging involving ionizing radiation is the risk of cancer induction. Radiation-induced cancer may occur at any time, including after decades, following the radiation exposure event, and, if it occurs, it is indistinguishable from spontaneously induced cancer.

The progressive understanding of biologic effects of radiation led to the development of guidelines for radiation protection by the international community. Evidence-based guidelines are outlined in the 2007 Recommendations of the International Commission for Radiological Protection (International Commission for Radiological Protection, 2007) and in the recommendations of the National Council on Radiation Protection and Measurements (NCRP) of the United States (Kase 2004).

The overarching goal of radiation protection in medical diagnostic imaging is to obtain a maximum of information relevant to the diagnostic task with the least amount of exposure to ionizing radiation (White & Pharoah, 2009). In practice, economic and individual factors, such as availability or access to imaging modalities of choice must also be taken into account.

The application in diagnostic imaging of this principle, also referred to "As Low As Reasonably Achievable" (ALARA), involves the implementation of general protective measures, including the following:

1. Imaging decision. Selection of the imaging examination to answer a specific diagnostic question should take into consideration all modalities that are likely to provide the sought information. When the diagnostic question can be answered through a study that involves no ionizing radiation - such as magnetic resonance or ultrasound imaging - the added radiation dose from the diagnostic procedure is reduced to zero. The selection of the imaging modality involving exposure to ionizing radiation should follow a justification process based on the patients' individual clinical circumstances and on scientific evidence. This process should suggest that the potential diagnostic benefit of the examination outweighs the estimated risk carried by the specific radiation exposure. Decision support software, which can assist the clinician in determining the appropriateness of a given imaging study to the clinical situation, has recently become available (Rosenthal et al., 2006). Preliminary studies have suggested that its utilization can contribute to the decreased prescription of examinations that are deemed of "low-utility" to the diagnostic task (Coakley et al., 2011).
2. Patient information: Providing easy-to-understand information to patients is an effective measure for bringing radiation exposure into context and for dispelling exaggerated fear of radiation in patients. Radiation doses from medical examinations can be compared with the amount of background radiation to which we are all exposed by living on Earth (see table 2). Risk comparison with common daily activities, such as driving or air travel, may also be effective (Coakley et al., 2011). For instance, travelling 64,000 km by car is associated with a risk of death from a motor vehicle accident of approximately 1:2000 in the United States (National Highway Traffic Safety Administration Fatality Analysis Reporting System, 2011). This risk is roughly equal to the risk of developing a fatal cancer from an effective radiation dose of 10 mSv, a dose five times higher than that from a typical CT scan of the head.

3. Shielding of the examination room, to limit or eliminate radiation exposure to neighbouring areas;
4. Shielding the patient's anatomic areas that are not in the region of interest of the examination, to reduce radiation exposure to sensitive organs, such as the thyroid, gonads, eye lens;
5. Filtration of the x-ray beam, which removes low energy photons that would otherwise be absorbed by the patient, and hence would not contribute to the radiographic image;
6. Optimal film-screen combinations that maximize photon-to-image conversion, while achieving the image quality required for the diagnostic task;
7. Appropriate x-ray source –to-skin distance, whenever this factor is adjustable;
8. Collimation of the exposed field strictly to the region of interest;
9. Optimal combination of exposure factors (kVp, mA, seconds) to achieve low radiation doses, while maintaining diagnostic image quality;
10. Quality assurance of the imaging and film processing equipment, to ensure consistent optimal quality of images with minimum exposure to patients and personnel.
11. Personal dose monitors and area dose monitors that assist in documenting individual exposure and area radiation levels. Personal dose monitors used in clinical practice include thermoluminescent dosimeters (TLD) and, more recently, optically stimulated dosimeters (OSLD). TLDs use lithium fluoride or calcium sulphate crystals laced with magnesium, titanium, copper or phosphorus impurities, which store the energy from radiation to which they are subjected. When the crystals are heated, the stored energy is released as luminescence proportional to the radiation exposure. While TLDs are small and they allow measurements of radiation doses ranging from microGy to kGy, accurate and reproducible readings are heavily technique-dependent (Kron 1994). OSLDs use aluminium oxide laced with carbon impurities to store radiation energy, which is released as luminescence proportional to the radiation exposure in response to stimulation light. OSLDs have a linear dose-response relationship in the 1-300 cGy range but can be calibrated for a significantly wider range of radiation exposures that are relevant in medical imaging (Jursinic 2007, Yukihara, 2008).

Due to the exponential growth in its utilization and its higher radiation effective dose compared to plain film radiographs, computed tomography (CT) is one of the most significant contributors to medical diagnostic radiation exposure today. While many of the general principles outlined above apply to CT as well, several measures specific to CT can be implemented to reduce patients' radiation risk:

1. Bismuth shields are used in the exposure path in front of sensitive organs, such as the breast. They partially absorb the direct radiation beam to underlying anatomic structures, without significantly impacting the image quality of adjacent structures. Bismuth shields can reduce radiation dose to the adult female breast by up to 40% (Yilmaz et al., 2007). However, when bismuth shields are used together with automatic exposure modulation, the latter may compensate for the radiation attenuation caused by the shield, offsetting the radiation savings benefits of the shield. To circumvent this situation, bismuth shields may be applied after exposure of the scout view, and before acquisition of the volumetric data (Coakley et al., 2011).
2. Optimization of CT imaging protocols involves tailoring imaging protocols to the patient and the diagnostic task. The radiation dose can be modified by adjusting one or several scan parameters:

i. The maximum tube electric potential (kVp): while the typical exposure setting used in routine CT scanning is between 100 and 140 kVp, a lower kVP can reduce radiation dose, albeit at the expense of increased image noise.
ii. Tube current (mA): a CT scan conducted with lower mA results in noisier images, but radiation exposure is diminished by an amount proportional to the decreased tube current.

Lower values can be selected for both parameters when scanning children or small adults, or in cases in which noisier images are unlikely to have a significant impact on the diagnostic task outcome (e.g. a study to evaluate renal calculi).

3. X-ray tube current modulation and automatic exposure control refer to systems in which the user (the radiologist, through the radiological technologist) indicates the desired level of image quality, based on which the CT software calculates the radiation output required to match that image quality in all regions of the scanned volume (McCollough et al., 2005). During acquisition of each sectional image, as the gantry rotates around the patient, angular tube current modulation works to modulate x-ray tube current to equalize the average photon flux reaching the detectors (x-, y-axis tube current modulation). As the patient progresses through the gantry, longitudinal (z-axis) tube current modulation acts to maintain constant image noise levels along the longitudinal axis of the patient as body regions with different attenuation properties are scanned (McCollough et al., 2005).
4. Enhanced CT reconstruction algorithms: most current CT scanners utilize reconstruction algorithms based on the filtered back-projection (FBP) method. When used in combination with low tube currents, this method tends to generate noisy images. The implicit radiation exposure threshold, below which the diagnostic image quality decreases to unacceptable levels, limits the potential for radiation savings with FBP reconstruction algorithms. Alternative solutions include iterative reconstruction algorithms, based on complex mathematical models that aim to correct the noise in images acquired with low tube currents. These algorithms are computation-intensive and lead to longer reconstruction times (Coakley et al., 2011). A recent, enhanced, iterative reconstruction method, known as adaptive statistical iterative reconstruction (ASIR), shows great promise for improved reconstruction speeds. Furthermore, by attempting to identify and correct for photon flux fluctuations that are unlikely to be caused by anatomic features, ASIR can reduce image noise, as well as certain types of image artefacts (Marin et al., 2010, Miéville et al., 2011, Renker et al., 2011). As a result, images reconstructed using ASIR from raw data acquired with low tube current may show similar or improved image quality compared to FBP reconstructions, while low current settings allow radiation savings in the range of 32-65% for a variety of clinical utilization scenarios (Cornfeld et al., 2011, Flicek et al., 2010, Hara et al., 2009). Together, these characteristics of ASIR protocols may lead to CT studies of overall similar or better diagnostic quality compared to FBP reconstruction methods, with a potential for significantly reduced patient radiation exposure.
5. Calculation and reporting of radiation dose: Most CT scanners have the integrated capability to calculate radiation exposure as a dose-length product (measured in mGy/cm), which can be recorded in the patient's clinical record. This facilitates tracking CT radiation exposure to patients.

3. Modelling and simulation for radiation control of imaging devices

3.1 Preliminaries

Automated control of radiation field intensity generated during medical imaging and radiation therapy, constitutes an efficient method to reduce unnecessary radiation exposure for both patients and device operators (Sajin et al., 2003, McCollough et al., 2006).

This heading presents an original method for automated control of radiation field intensity. Its implementation in medical imaging devices employing ionizing radiation can offer important exposure savings to both patients and medical personnel.

The goal of this study has been to develop an original and flexible model for radiation field control, in order to allow an exact administration of the minimum necessary radiation dose at any desired tissue depth, even through non-homogeneous tissue layers that intensify or attenuate the electromagnetic field generated by an imaging device. Therefore, we modelled and simulated the spread of radiation through non-homogeneous media, as is the case when using medical imaging devices to investigate human tissues.

A general model of radiation field spread using Cartesian coordinates (0p; 0q; 0r) can be represented as seen in figure 1. Patterns of spread have been considered, in relation to three spatial axes and in relation to time (t).

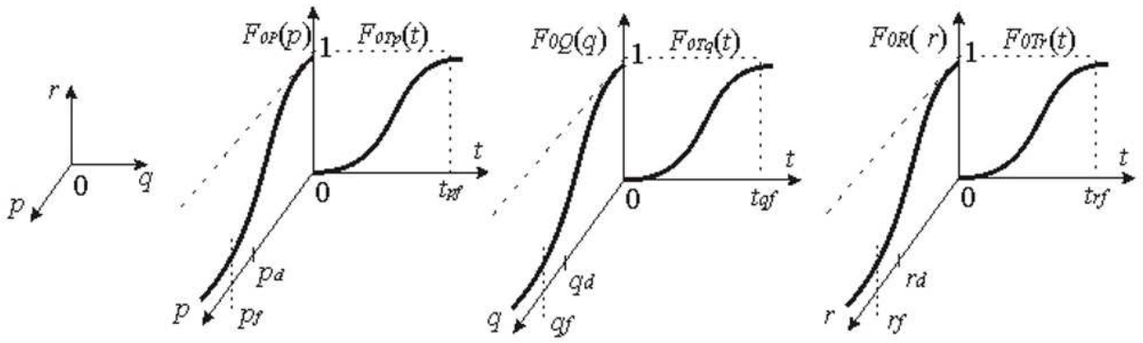

a. y on 0p axis **b.** y on 0q axis; **c.** y on 0r axis

Fig. 1. General model of radiation field intensity, y(t, p, q, r) in Cartesian coordinates

Radiation field intensity y(t, p, q, r) shown in figures 1b, 1c, and 1d, can be expressed as:

$$y(t,p,q,r)=y_{00}[t,s,u(t)]=K_y \times F_{0T}(t) \times F_{0S}(s) \times u(t) \quad (1)$$

The output variable y=y[t, s, u(t)] is the intensity of the radiation field, u(t) is the input (command) signal applied for the radiation source, Ky is a weighting coefficient and (2) stands for the usual form of compression of the Cartesian space variable on the axes of coordinates (0p), (0q) and (0r), as illustrated in figure 2.

$$s = \pm\sqrt{p^2+q^2+r^2}\,; \quad s_f = \pm\sqrt{p_f{}^2+q_f{}^2+r_f{}^2} \quad (2)$$

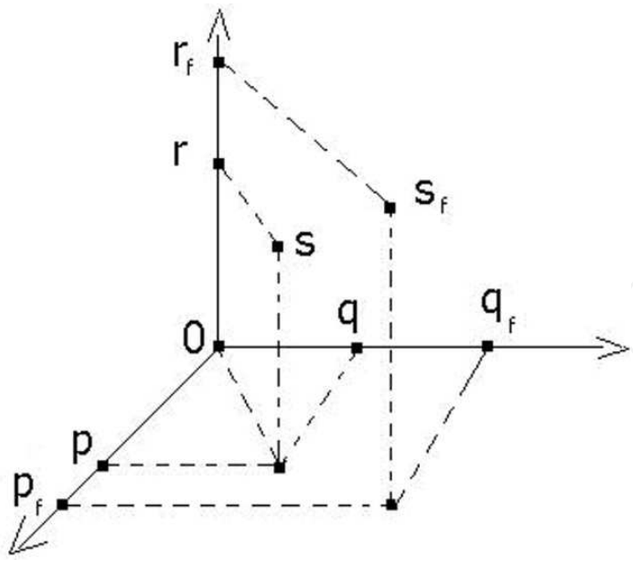

Fig. 2. Cartesian coordinates system and Cartesian space variable (s)

$$F_{0S}(s)=\pm\sqrt{F_{0P}^{\ 2}(p)+F_{0Q}^{\ 2}(q)+F_{0R}^{\ 2}(r)} \tag{3}$$

where:

$$F_{0P}(p)=\frac{P_1}{P_1-P_2}\times\varepsilon^{-\frac{abs(p)}{P1}}+\frac{P_2}{P_2-P_1}\times\varepsilon^{-\frac{abs(p)}{P2}} \tag{4}$$

$$F_{0Q}(q)=\frac{Q_1}{Q_1-Q_2}\times\varepsilon^{-\frac{abs(q)}{Q1}}+\frac{Q_2}{Q_2-Q_1}\times\varepsilon^{-\frac{abs(q)}{Q2}} \tag{5}$$

$$F_{0R}(r)=\frac{R_1}{R_1-R_2}\times\varepsilon^{-\frac{abs(r)}{R1}}+\frac{R_2}{R_2-R_1}\times\varepsilon^{-\frac{abs(r)}{R2}} \tag{6}$$

The axes (0p) and (0q) define the horizontal plane, in which the electromagnetic field generator is located. Field intensity expressed in (1), and axis (0r) correspond to the depth of field propagation. The constants in (4), (5) and (6) can be approximated by expert procedures, namely:

$$P_1=\frac{p_f}{\mu_P(1+\lambda_P)}\ ;\ P_2=\lambda_P\times P_1\ ,\ \text{where: } \mu_P=(4\div6)\ \text{and}\ \lambda_P>1 \tag{7}$$

$$Q_1=\frac{q_f}{\mu_Q(1+\lambda_Q)}\ ;\ Q_2=\lambda_Q\times Q_1\ ,\ \text{where: } \mu_Q=(4\div6)\ \text{and}\ \lambda_Q>1 \tag{8}$$

$$R_1=\frac{r_f}{\mu_R(1+\lambda_R)}\ ;\ R_2=\lambda_R\times R_1\ ,\ \text{where: } \mu_R=(4\div6)\ \text{and}\ \lambda_R>1 \tag{9}$$

in which the final abscises (p_f), (q_f), (r_f) correspond to negligible values (for example ≤ 0.05). For $F_{0P}(p)$, $F_{0Q}(q)$, $F_{0R}(r)$, the abscises (p_d), (q_d), (r_d) may show disturbances due to discontinuities in tissue structure, estimated by:

$$F_{0S}(s)=\frac{S_1}{S_1-S_2}\times\varepsilon^{-\frac{abs(s)}{S1}}+\frac{S_2}{S_2-S_1}\times\varepsilon^{-\frac{abs(s)}{S2}} \tag{10}$$

where

$$S_1=\frac{s_f}{\mu_S\times(1+\lambda_S)}\;;\quad S_2=\lambda_S\times S_1 \tag{11}$$

$$\mu_S=\frac{p_f+q_f+r_f}{\frac{p_f}{\mu_P}+\frac{q_f}{\mu_Q}+\frac{r_f}{\mu_R}}\;;\quad \lambda_S=\frac{P_2+Q_2+R_2}{P_1+Q_1+R_1} \tag{12}$$

Therefore, $F_{0S}(s)$ can also be written:

$$F_{0S}(s)=\frac{1}{1-\lambda_S}\times\left[\varepsilon^{-\frac{\mu S(1+\lambda S)}{sf}\times abs(s)}-\lambda_S\times\varepsilon^{-\frac{\mu S(1+\lambda S)}{sf}\times abs(s)}\right] \tag{13}$$

or

$$F_{0S}(s)=C_0\times\left(\varepsilon^{C1\times\sqrt{p^2+q^2+r^2}}+C_2\times\varepsilon^{C3\sqrt{p^2+q^2+r^2}}\right) \tag{14}$$

in which

$$C_0=\frac{1}{1-\lambda_S}\;;\quad C_1=\frac{\mu_S(1+\lambda_S)}{s_f}\;;\quad C_2=-\lambda_S\;;\quad C_3=\frac{1}{\lambda_S}\times C_1 \tag{15}$$

The results of $F_{0S}(s)$ in (4), (10), (13) and (14) also represent spatial curves deformed by multiple degrees of freedom, for example (μ_S), (λ_S) and (s_f), while the "length constants" (P…), (Q…) and (R…) may exhibit "inertia" or "attenuation" of radiation field propagation through different tissue layers.

Function components $F_{0P}(p)$, $F_{0Q}(q)$ or $F_{0R}(r)$ can be approximated by:

$$F_{0vd}(v)=A_{vd}\times\varepsilon^{-Kvd(vd-v)^2} \tag{16}$$

in which variable (v) becomes (p), (q) or (r), according to case.

The disturbance index (d) refers to the homogeneity disturbance due to tissue heterogeneity located on the abscissa (v_d), while (A_{vd}) in (16) represents the amplitude of heterogeneity illustrated in figure 3.a.

A more or less steep, respectively a more or less symmetrical slope can result from the convenient choice of parameter (K_{vd}). The deformation effect of function $F_{0vd}(v)$ on the right abscissa (v_d) over the component $F_{0v}(v)$ can be seen in figure 3.b.

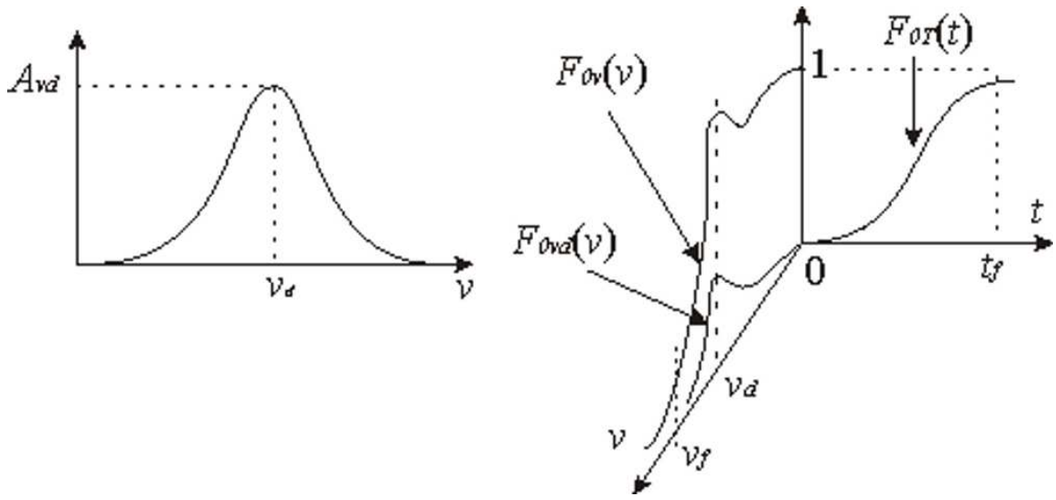

a. Amplitude **b.** Trajectory in Cartesian space

Fig. 3. Tissue heterogeneity may lead to homogeneity disturbances of field intensity

If, with respect to time, the spread of radiation field intensity y(t,p,q,r) is identical on all three axes (0p), (0q) and (0r) depicted in figures 1a, 1b and 1c, then:

$$F_{0Tp}(t)=F_{0Tq}(t)=F_{0Tr}(t)=F_{0T}(t) \tag{17}$$

which may also be approximated as a customary form of step response, related to a control signal u(t) applied to the radiation source.

Thus:

$$F_{0T}(t)=1-\frac{T_1}{T_1-T_2}\times\varepsilon^{-\frac{t}{T1}}-\frac{T_2}{T_2-T_1}\times\varepsilon^{-\frac{t}{T2}} \tag{18}$$

The final values (p_f, q_f, r_f, v_f) in figures 1a, 1b, 1c, 2 and 3 show the depth of radiation field penetration, which will depend on this control signal u(t) and on the more or less homogeneous structure of the tissue. The length (t_f) of this transient phenomenon (figure 4) reflects a radiation propagation inertia, identical on axes (p, q, r, s) for which $t>t_f$ tends to a unitary asymptote.

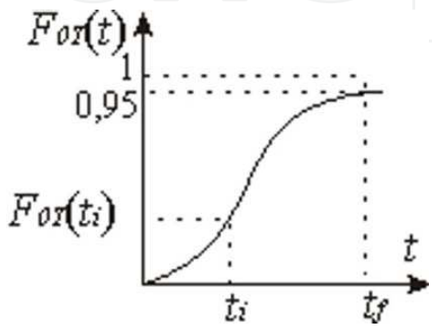

Fig. 4. Transient phenomenon

For a slow to fast ascending evolution we considered $\mu_T \cong 4 \div 6$, $\lambda_T > 1$, resulting in the following time constants:

$$T_1 = \frac{t_f}{\mu_T \times (1+\lambda_T)}; \quad T_2 = \lambda_T \times T_1; \quad t_i = \frac{T_1 \times T_2}{T_2 - T_1} \times \ln\left(\frac{T_2}{T_1}\right) \tag{19}$$

where (t_i) is the moment corresponding to the inflexion $F_{0\tau}(t_i)$.

If, with respect to time, the spread of radiation field intensity y(t,p,q,r) is not identical on all three axes (0p), (0q) and (0r) depicted in figures 1a, 1b and 1c, then condition (17) is no longer accomplished, resulting in:

$$F_{0Tp}(t) \neq F_{0Tq}(t) \neq F_{0Tr}(t) \tag{20}$$

In this case, formally identical to relation (19), each axis will exhibit:

$$T_{1p} = \frac{t_{pf}}{\mu_{Tq} \times (1+\lambda_{Tp})}; \quad T_{2p} = \lambda_{Tp} \times T_{1p} \tag{21}$$

$$T_{1q} = \frac{t_{qf}}{\mu_{Tq} \times (1+\lambda_{Tq})}; \quad T_{2q} = \lambda_{Tq} T_{1q} \tag{22}$$

$$T_{1r} = \frac{t_{rf}}{\mu_{Tr} \times (1+\lambda_{Tr})}; \quad T_{2r} = \lambda_{Tr} T_{1r} \tag{23}$$

where (t…f), (μ_T…) and (λ_T…) are specifically established for each axis.

In order to transform into Cartesian coordinates it can be shown that:

$$\mu_\tau = \frac{t_{pf} + t_{qf} + t_{rf}}{T_{1p} + T_{2p} + T_{1q} + T_{2q} + T_{1r} + T_{2r}}; \quad \lambda_\tau = \frac{T_{2p} + T_{2q} + T_{2r}}{T_{1p} + T_{1q} + T_{1r}} \tag{24}$$

finally resulting in:

$$T_1 = \frac{t_f}{\mu_\tau \times (1+\lambda_\tau)}; \quad T_2 = \lambda_\tau \times T_1 \tag{25}$$

which are the equivalent time constants of the Cartesian space, assuming that inertial propagations are different along the three axes (p, q, r).

Following this method, $F_{0T}(t)$ in equation (1) becomes:

$$F_{0T}(t) = \frac{T_1}{T_1 - T_2} \times \varepsilon^{-\frac{t}{T1}} + \frac{T_2}{T_2 - T_1} \times \varepsilon^{-\frac{t}{T2}} \tag{26}$$

which together with $F_{0S}(s)$ from (10), allows the computation of the radiation field intensity defined by (1) and depicted in figure (1).

3.2 Analogical modelling

Figure 5 presents the proposed control block diagram for adjusting radiation fields. It's components have been modeled by algebraic and differential equation systems (27) and (28), as well as by partial differential equation (29).

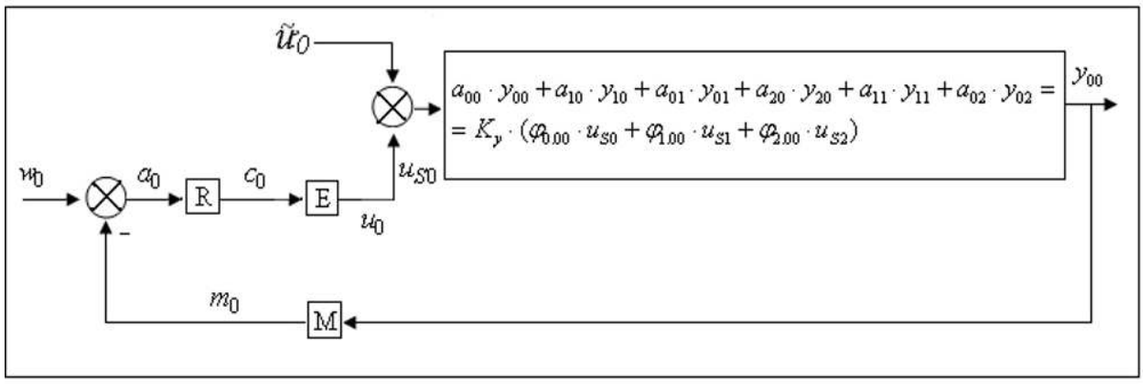

Fig. 5. Control block diagram of the proposed adjustment system

$$a_0 = w_0 - m_o \; ; \quad K_m \times y_{00} = m_0 + T_m \times m_1 \tag{27}$$

$$K_{IR} \times a_0 + K_{PR} \times a_1 + K_{DR} \times a_2 = c_1 + T_R \times c_2 \sqrt{a^2 + b^2} \; ; \quad K_E \times c_0 = u_0 + T_E \times u_1 \tag{28}$$

$$a_{00} \times y_{00} + a_{10} \times y_{10} + a_{01} \times y_{01} + a_{20} \times y_{20} + a_{11} \times y_{11} + a_{02} \times y_{02} = K_y \times (\varphi_{0.00} \times u_{S0} + \varphi_{1.00} \times u_{S1} + \varphi_{2.00} \times u_{S2}) \tag{29}$$

The indexes in relations (27), (28) and the first parameter in relation (29), correspond to the order of derivative with respect to time (t). The second parameter in (29) corresponds to the order of derivative with respect to variable (s), defined in relation (2).

The radiation field intensity (y_{00}) defined by (1) is converted by the measurement transducer M into electrical signal (m_0) found in (27). The control error (a_0) results from (27), in which (w_0) is the reference signal.

In the above presented adjustment scheme, the R controller with proportional integrative derivative (PID) behaviour defined in (28) emits a control signal (c_0) which adjusts the electromagnetic field generator E, as defined in relation (28).

The radiation emitting unit, E, generates the execution signal (u_0) representing the incident radiation field applied to various environments (e.g. air, tissues), together with a resultant disturbance signal ($\tilde{u}_0$), resulting in:

$$u_{S0} = u_0 \pm \tilde{u}_0 \tag{30}$$

In the above equation, (u_{S0}) is the resulted electromagnetic field and ($\tilde{u}_0$) corresponds to the homogeneity disturbance $F_{ovd}(v)$ from (16), where $v = s_d$, which may be defined in Cartesian space as seen in figure 6 and expressed in (31).

$$t_f=\sqrt{t_{pf}^2+t_{qf}^2+t_{rf}^2}\ ;\ \ s_f=\sqrt{p_f^2+q_f^2+r_f^2}\ ;\ \ s_d=\sqrt{p_d^2+q_d^2+r_d^2} \tag{31}$$

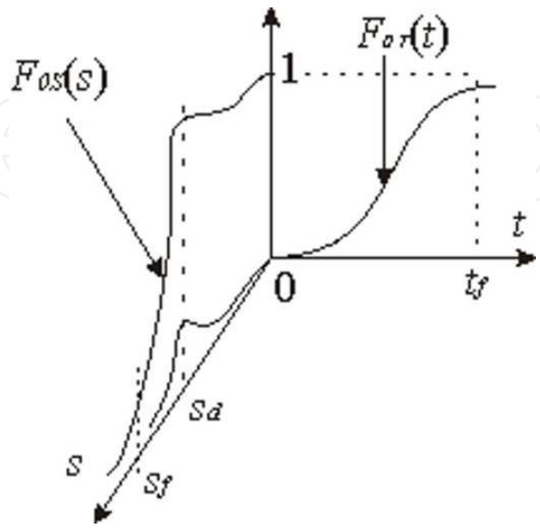

Fig. 6. F_{OT} and F_{OS} including homogeneity disturbance at s_d

Thus, the complex phenomenon of radiation spread can be estimated and adjusted by partial differential equation (29).

In the left side of this equation we introduced the approximated solution

$$y_{00}[t,s,u(t)]=K_y\times F_{00}(t,s)\times u_{S0}(t) \tag{32}$$

where $F_{00}(t,s)=F_{0T}(t)\times F_{0S}(s)$ and (K_y) is a weighting coefficient.

This resulted for the right side of equation (29) in:

$$\varphi_{0.00}=a_{00}\times F_{00}+a_{10}\times F_{10}+a_{01}\times F_{01}+a_{20}\times F_{20}+a_{11}\times F_{11}+a_{02}\times F_{02} \tag{33}$$

$$\varphi_{01.00}=a_{10}\times F_{00}+2\times a_{20}\times F_{10}+a_{11}\times F_{01} \tag{34}$$

$$\varphi_{2.00}=a_{20}\times F_{00} \tag{35}$$

in which partial derivatives ($F_{0...}$), (F_{11}) and ($F_{...0}$) are obtained from (32). Only signal (u_0) is included in the block diagram. The homogeneity disturbance ($\tilde{u}_0$) is an independent external signal.

From the equation system (27)…(31), the matrix containing partial derivatives of the state vector (M_{dpx}) represented in (36) has been deduced for the entire adjustment system depicted in figure 5.

$$\mathbf{M}_{dpx} = \begin{array}{|c|c|}\hline x & x_S \\ \hline x_T & x_{TS} \\ \hline \end{array} = \begin{array}{|c|cccc|}\hline m_0 & & & 0 & \\ m_1 & & & 0 & \\ c_0 & & & 0 & \\ c_1 & & & 0 & \\ u_0 & & & 0 & \\ u_1 & & & 0 & \\ y_{00} & y_{01} & y_{02} & \ldots & y_{08} \\ y_{10} & y_{11} & y_{12} & \ldots & y_{18} \\ \hline m_2 & & & 0 & \\ c_2 & & & 0 & \\ u_2 & & & 0 & \\ y_{20} & y_{21} & y_{22} & \ldots & y_{28} \\ \hline m_3 & & & 0 & \\ c_3 & & & 0 & \\ u_3 & & & 0 & \\ y_{30} & y_{31} & y_{32} & \ldots & y_{38} \\ \hline & & \ldots & & \\ \hline m_6 & & & 0 & \\ c_6 & & & 0 & \\ u_6 & & & 0 & \\ y_{60} & y_{61} & y_{62} & \ldots & y_{68} \\ \hline \end{array} \quad (36)$$

Because the signals m=m(t), c=c(t) and u=u(t) are functions only of time, all their partial derivatives with respect to (s) are equal to zero. Details concerning analogical modelling of systems through $\left(M_{dpx}\right)$ may be found in T. Colosi et al., 2009.

3.3 Numerical simulation

Numerical simulation has been performed using $\left(M_{dpx}\right)$ and Taylor series, which required knowledge of initial conditions CI(t_0,s), for $x_{CI}=x(t_0,s)=x_{k-1}$. Hence, by partial derivative with respect to (s), $x_{S,CI}=x_s(t_0,s)=x_{S,k-1}$, in which sequence (k-1) corresponds to the moment $t_{k-1}=(k-1)\times\Delta t$, and sequence (k) corresponds to $t_k=k\times\Delta t$, where (Δt) is a sufficiently small integration step.

By means of $\left(x_{CI}\right)$ and $\left(x_{S,CI}\right)$ we computed the composing elements of $\left(x_T\right)$ and $\left(x_{TS}\right)$, using specific operations based on symbolic derivatives by indices: $x_{T,CI}=x_T\left(t_0,s\right)=x_{T,k-1}$ and $x_{TS,CI}=x_{TS}\left(t_0,s\right)=x_{TS,k-1}$.

After setting these initial conditions, we approximated through iterative calculus:

$$x_k=x_{k-1}+\sum_{T=1}^{6}\frac{\Delta t^T}{T!}\times x_{T,k-1}\ ; \qquad x_{S,k}=x_{S,k-1}+\sum_{T=1}^{6}\frac{\Delta t^T}{T!}\times x_{TS,k-1} \quad (37)$$

For each integration step (Δt) we operated with a number of 20 Taylor series, of which 6 for ($m_{0k}, m_{1k}, c_{0k}, c_{1k}, u_{0k}, u_{1k}$) and 14 for ($y_{00k}, y_{01k}, ..., y_{06k}$).

It can be observed that 8 elements (signals) included in Taylor series are from the state vector component (x) while the other 12 are from the matrix component (x_S), all of them included in (M_{dpx}).

The truncation error at each integration step (Δt) is proportional to $(\Delta t^7 / 7!)$, for (m, c, u, y_{00}), as well as to $(\Delta t^6 / 6!)$, for (y_{10}).

3.4 Examples of simulated radiation control

In order to illustrate the radiation control that would result from an electronic implementation of the above adjustment system, we present the simulated results regarding field intensity and its automatic adjustment for three simulated tissue types:

1. homogenous tissue
2. **heterogeneous** tissue with an intensity-**increasing** homogeneity disturbance located between body surface and the tissue depth targeted for imaging
3. **heterogeneous** tissue with both an intensity-**decreasing** and an intensity-**increasing** homogeneity disturbance, located between body surface and the targeted tissue depth

For every case, the intensity and spread of electromagnetic radiation has been simulated in open loop (without radiation field control) and in closed loop (with radiation field control).

In all simulated cases the adjustment goal was to ensure a predefined, constant and uniform intensity level of 5 units (e.g. 5 mGy) at a tissue depth of 50 units (e.g. 50 mm), regardless of potential intensity disturbers (radiation absorbing or intensifying environments) localized between body surface and the targeted tissue depth of 50 units.

Numerical simulation was performed using Matlab 7.5.0.

Since our goal has been to develop a general model, we did not impose certain scales or units of measurement. The scales and units of measurement constitute flexible choices that may be conveniently defined for every imaging technique for which our method would be implemented. Given that initialization parameters need to be conveniently chosen and experimentally calibrated for every targeted imaging technique (CT, cone-beam CT, conventional radiography, etc.), we will not undergo a presentation regarding the initial parameters used for these simulated examples. Details regarding the choice of these initial parameters may be found in Roman et al., 2009, 2010 and Colosi et al., 2010.

Simulation results regarding field intensity have been plotted against time and tissue depth, as seen in figures 7-12. Colour coding has been employed in order to highlight different intensity levels of the electromagnetic radiation field.

For every simulated case (figures 7 and 8; figures 9 and 10; figures 11 and 12), significant changes regarding electromagnetic field intensity at different tissue depth can be observed between the unadjusted systems and the ones adjusted by the PID controller.

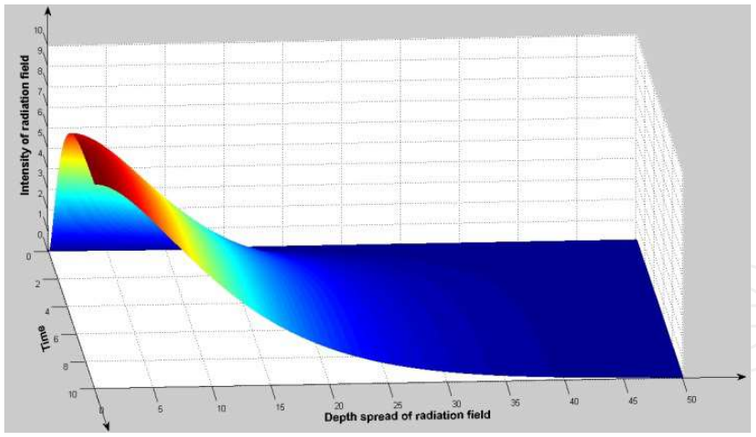

Fig. 7. Intensity of the electromagnetic radiation field, simulated in open loop (without radiation field adjustment), for a homogenous tissue.

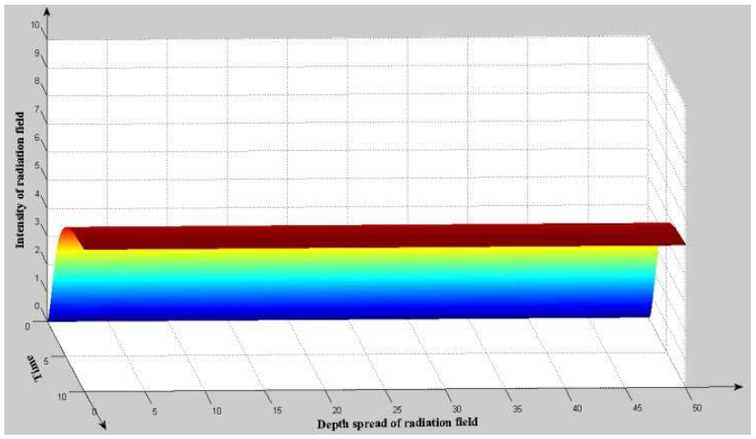

Fig. 8. Adjustment of the electromagnetic radiation field towards a constant intensity of 5 units at a tissue depth of 50 units, simulated in closed loop, for a homogenous tissue.

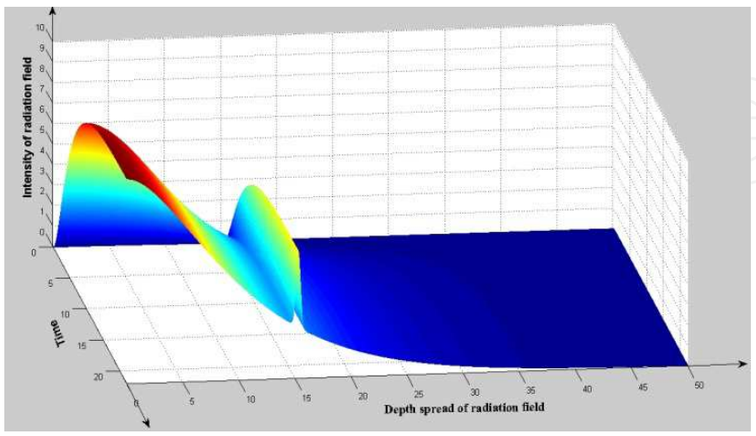

Fig. 9. Intensity of the electromagnetic radiation field, simulated in open loop (without radiation field adjustment), for a heterogeneous tissue with an intensity-increasing homogeneity disturbance at a depth of 15 units.

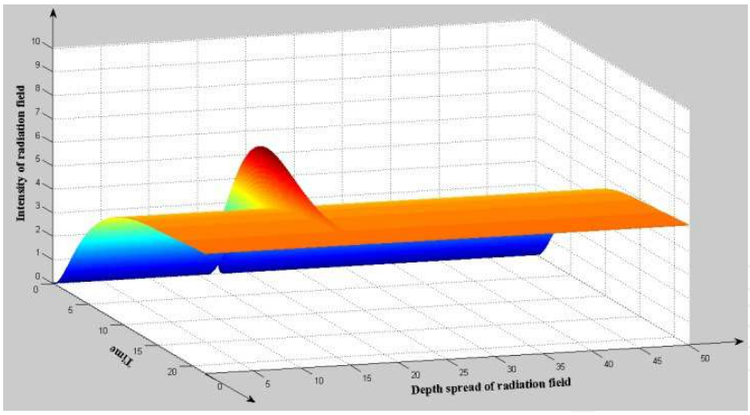

Fig. 10. Adjustment of the electromagnetic radiation field towards a constant intensity of 5 units at a tissue depth of 50 units, simulated in closed loop, for a heterogeneous tissue with an intensity-increasing homogeneity disturbance at a depth of 15 units.

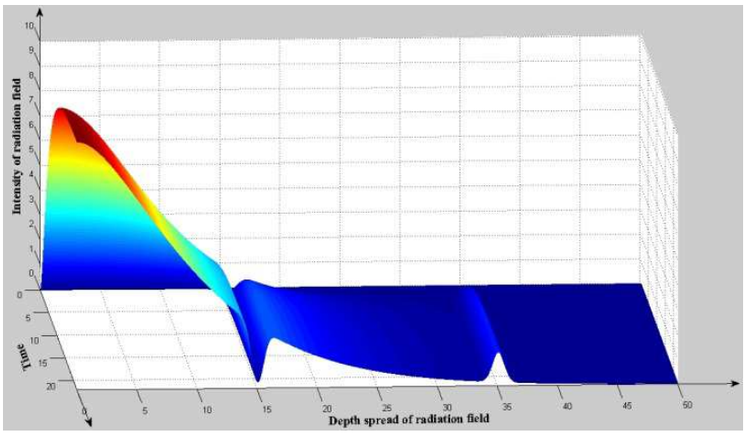

Fig. 11. Intensity of the electromagnetic radiation field, simulated in open loop (without radiation field adjustment), for a heterogeneous tissue with an intensity-decreasing homogeneity disturbance at a depth of 15 units and an intensity-increasing homogeneity disturbance at a depth of 35 units.

Figures 7, 9 and 11 illustrate the fact that, due to radiation absorption from a dense environment, an unadjusted systems can not achieve the targeted dose of 5 intensity units at the desired depth of 50 units, unless a significantly higher field intensity is administered to begin with.

On the other hand, when the systems are adjusted by the PID controller, the electromagnetic field intensity at a tissue depth of 50 units is stabilized at the targeted value of 5 units, in all simulated cases.

Thus, the controlled systems in figures 8, 10 and 12 ensure a minimization of the total administered radiation dose necessary to achieve 5 intensity units at 50 units of tissue depth.

As may be inferred from the examples above, this general and highly flexible model offers a foundation for very precise electromagnetic field adjustments. Experimental validation and calibration for concrete imaging techniques, as well as an electronic implementation of the model, remain to be performed in order to implement this model for practical use.

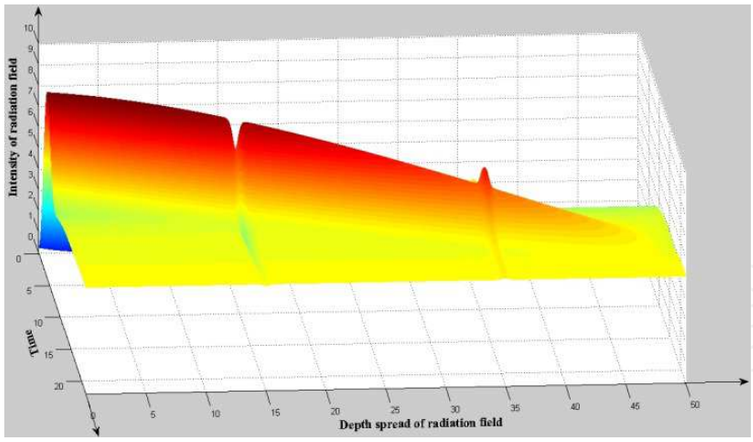

Fig. 12. Adjustment of the electromagnetic radiation field towards a constant intensity of 5 units at a tissue depth of 50 units, simulated in closed loop, for a heterogeneous tissue with an intensity-decreasing homogeneity disturbance at a depth of 15 units and an intensity-increasing homogeneity disturbance at a depth of 35 units.

4. Conclusion

The proposed radiation adjustment model offers a precise tool to assist in meeting the overarching goal of radiation protection: to obtain a maximum of relevant imaging information, with the least amount of exposure to ionizing radiation.

5. References

Brenner, D.J. & Hall, E.J. (2007). Computed Tomography — An Increasing Source of Radiation Exposure. *New England Journal of Medicine*, Vol. 357, No. 22, pp.2277-2284, ISSN 0028-4793.

Coakley, F.V. et al. (2011). CT radiation dose: what can you do right now in your practice? AJR. American *Journal of Roentgenology*, Vol. 196, No. 3, pp.619-625, ISSN 1546-3141.

Colosi, H. & Roman, N.M. (2010). Digital Simulation and Control of Electromagnetic Field Effects in Heterogeneous Organic Tissues, *Proceedings of 2010 IEEE International Conference on Automation, Quality and Testing, Robotics,* pp. 321-326, ISBN 978-1-4244-6722-8, Cluj-Napoca, Romania, May 28-30, 2010

Colosi, T.; Ungureşan, M.L.; Dulf, E.H. & Cordoş, R.C. (2009). *Introduction to Anlogical Modeling and Numerical Simulation, with (Mpdx) and Taylor Series for Distributed Parameters Processes*, Ed. Galaxia Gutenberg, ISBN 978-973-141-192-7, Târgu-Lăpuş, Romania

Cornfeld, D. et al. (2011). Impact of Adaptive Statistical Iterative Reconstruction (ASIR) on Radiation Dose and Image Quality in Aortic Dissection Studies: A Qualitative and Quantitative Analysis. *Am. J. Roentgenol.*, Vol. 196, No. 3, pp.W336-340.

Flicek, K.T. et al. (2010). Reducing the radiation dose for CT colonography using adaptive statistical iterative reconstruction: A pilot study. *American Journal of Roentgenology*, Vol. 195, No. 1, pp.126-131, ISSN 1546-3141.

Hall, E.J. & Giaccia, A.J. (2005). *Radiobiology for the Radiologist.* (6th ed.), ISBN 978-0781741514 Lippincott Williams & Wilkins Publishing, Philadelphia, PA.

Hara, A.K. et al. (2009). Iterative reconstruction technique for reducing body radiation dose at CT: feasibility study. AJR. American Journal of Roentgenology, Vol. 193, No. 3, pp.764-771, ISSN 1546-3141

International Commission on Radiological Protection, 2007. The 2007 Recommendations of the International Commission on Radiological Protection. ICRP publication 103. Annals of the ICRP, 37(2-4), pp.1-332.

Jursinic, P.A., 2007. Characterization of optically stimulated luminescent dosimeters, OSLDs, for clinical dosimetric measurements. Medical Physics, 34(12), pp.4594-4604.

Kase, K.R., 2004. Radiation protection principles of NCRP. Health Physics, 87(3), pp.251-257.

Kron, T., 1994. Thermoluminescence dosimetry and its applications in medicine--Part 1: Physics, materials and equipment. Australasian Physical & Engineering Sciences in Medicine / Supported by the Australasian College of Physical Scientists in Medicine and the Australasian Association of Physical Sciences in Medicine, 17(4), pp.175-199.

Marin, D. et al. (2010). Low-Tube-Voltage, High-Tube-Current Multidetector Abdominal CT: Improved Image Quality and Decreased Radiation Dose with Adaptive Statistical Iterative Reconstruction Algorithm—Initial Clinical Experience1. *Radiology*, Vol. 254, No. 1, pp.145 -153

McCollough, C.H., Bruesewitz, M.R. & Kofler, J.M., Jr, (2006). CT dose reduction and dose management tools: overview of available options. Radiographics: *A Review Publication of the Radiological Society of North America*, Inc, Vol. 26, No. 2, pp.503-512, ISSN 1527-1323

Miéville, F.A. et al. (2011). Paediatric cardiac CT examinations: impact of the iterative reconstruction method ASIR on image quality - preliminary findings. *Pediatric Radiology*. Available at: http://www.ncbi.nlm.nih.gov/pubmed/21717165 [Accessed July 1, 2011]. ISSN 1432-1998

Mladenov, E. & Iliakis, G. (2011). Induction and repair of DNA double strand breaks: The increasing spectrum of non-homologous end joining pathways. *Mutation Research*, Vol. 711 No. 1-2, pp.61-72, ISSN 0027-5107

National Highway Traffic Safety Administration Fatality Analysis Reporting System, Fatality Analysis and Reporting System Encyclopedia. *National Highway Traffic Safety Administration Fatality Analysis Reporting System.* Available at: http://www-fars.nhtsa.dot.gov/Main/index.aspx [Accessed July 1, 2011].

Renker, M. et al. (2011). Evaluation of Heavily Calcified Vessels with Coronary CT Angiography: Comparison of Iterative and Filtered Back Projection Image Reconstruction. *Radiology*. Available at: http://www.ncbi.nlm.nih.gov/pubmed/21693660 [Accessed July 1, 2011], ISSN 1527-1315

Roman, N.M.; Colosi, H. & Pusca, M. (2009). Digital Simulation for Computer Control of Radiological Devices: A Preliminary Model Using Partial Differential Equations, *Proceedings of MediTech 2009 International Conference on Advancements of Medicine and Health Care through Technology,* pp. 37-42, ISBN 978-3-642-04291-1, Cluj-Napoca, Romania, September 23-26, 2009

Roman, N.M.; Colosi, H. & Pusca, M. (2010). Numerical Simulation Using Partial Differential Equations for Modeling and Control of Medical Radiation Fields.

Annals of the Academy of Romanian Scientists, Series on Science and Technology of Information, Vol.3, No.1, (2010), pp. 59-74, ISSN 2066-2742

Ron, E. (2003). Cancer risks from medical radiation. *Health Physics*, 85(1), pp.47-59, ISSN 0017-9078

Rosenthal, D.I. et al. (2006). Radiology order entry with decision support: initial clinical experience. *Journal of the American College of Radiology*. Vol. 3, No. 10, pp.799-806, ISSN 1558-349X

Sajin, G.; Sajin, M. & Gavriloaia, G. (2003). *Aplicații biologice ale radiațiilor electro-magnetice*, Ed. Academiei Tehnice Militare, ISBN 973-640-010-7, Bucureşti, Romania

United Nations Scientific Committee on the Effects of Atomic Radiation (2010). *Sources and Effects of Ionizing Radiation. [UNSCEAR] 2008 Report to the General Assembly with Scientific Annexes (2010): Vol. 1 Annex A*. United Nations Publications, ISBN 978-92-1-142274-0 New York, NY

United Nations Scientific Committee on the Effects of Atomic Radiation (2010). *Sources and Effects of Ionizing Radiation. [UNSCEAR] 2008 Report to the General Assembly with Scientific Annexes (2010): Vol. 1 Annex B.* United Nations Publications, ISBN 978-92-1-142274-0 New York, NY

White, S.C. & Pharoah, M.J. (2009). *Oral Radiology - Principles and Interpretation* (6th ed.), Mosby Elsevier ISBN 978-0323049832 St. Louis, MO

Yilmaz, M.H. et al. (2007). Female breast radiation exposure during thorax multidetector computed tomography and the effectiveness of bismuth breast shield to reduce breast radiation dose. *Journal of Computer Assisted Tomography*, Vol. 31, No. 1, pp.138-142, ISSN 0363-8715

Yukihara, E.G. & McKeever, S.W.S., 2008. Optically stimulated luminescence (OSL) dosimetry in medicine. Physics in Medicine and Biology, 53(20), pp.R351-379.

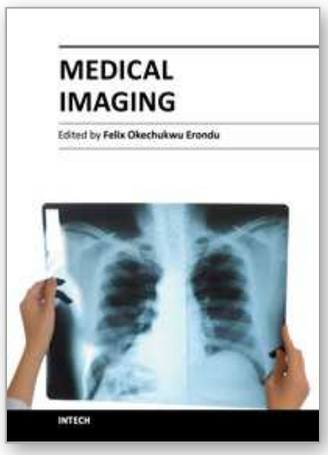

Medical Imaging

Edited by Dr. Okechukwu Felix Erondu

ISBN 978-953-307-774-1
Hard cover, 412 pages
Publisher InTech
Published online 22, December, 2011
Published in print edition December, 2011

What we know about and do with medical imaging has changed rapidly during the past decade, beginning with the basics, following with the breakthroughs, and moving on to the abstract. This book demonstrates the wider horizon that has become the mainstay of medical imaging sciences; capturing the concept of medical diagnosis, digital information management and research. It is an invaluable tool for radiologists and imaging specialists, physicists and researchers interested in various aspects of imaging.

How to reference

In order to correctly reference this scholarly work, feel free to copy and paste the following:

Horaţiu Colosi, Dan Colosi, Vlad Mureşan and Marius Roman (2011). Radiation Protection in Medical Imaging, Medical Imaging, Dr. Okechukwu Felix Erondu (Ed.), ISBN: 978-953-307-774-1, InTech, Available from: http://www.intechopen.com/books/medical-imaging/radiation-protection-in-medical-imaging

INTECH
open science | open minds

InTech Europe
University Campus STeP Ri
Slavka Krautzeka 83/A
51000 Rijeka, Croatia
Phone: +385 (51) 770 447
Fax: +385 (51) 686 166
www.intechopen.com

InTech China
Unit 405, Office Block, Hotel Equatorial Shanghai
No.65, Yan An Road (West), Shanghai, 200040, China
中国上海市延安西路65号上海国际贵都大饭店办公楼405单元
Phone: +86-21-62489820
Fax: +86-21-62489821

IntechOpen